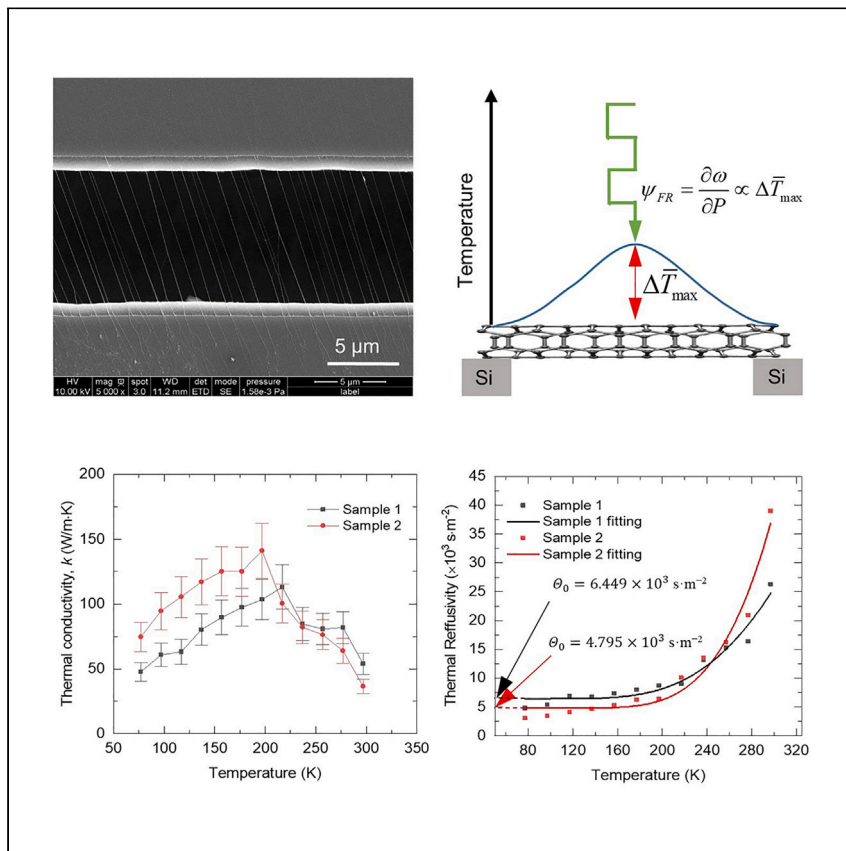Article

Observing grain boundary-induced phonons mean free path in highly aligned SWCNT bundles by low-momentum phonon scattering

Mahya Rahbar, Baini Li, Nicholas Hunter, Ibrahim Al Keyyam, Tianyu Wang, Enzheng Shi, Xinwei Wang

wangtianyu79@westlake.edu.cn (T.W.)
shienzheng@westlake.edu.cn (E.S.)
xwang3@iastate.edu (X.W.)

Highlights

Thermal diffusivity and conductivity of sub-7-nm SWCNT bundles is measured

SWCNT bundles can be examined in the axial direction down to 77 K

Residual thermal reffusivity is determined at 0 K, corresponding to the defect level

The structure thermal domain size of SWCNTs is shown to be approximately 46–62 nm

Due to their extremely small cross-sectional area, traditional beam-scattering techniques are not able to characterize the crystallite size of single-walled carbon nanotubes. Here, Rahbar et al. show that thermal domain size provides critical insight into the axial direction of structural characteristics of the nanotubes, which is of importance for material design.

Cell Reports
Physical Science

Article

Observing grain boundary-induced phonons mean free path in highly aligned SWCNT bundles by low-momentum phonon scattering

Mahya Rahbar,[1,3] Baini Li,[2,3] Nicholas Hunter,[1] Ibrahim Al Keyyam,[1] Tianyu Wang,[2,*] Enzheng Shi,[2,*] and Xinwei Wang[1,4,*]

SUMMARY

Due to their nanoscale scattering cross section, single-walled carbon nanotubes (SWCNTs) have never been reported for crystallite size or similar characteristics. Here, we characterize the average structure thermal domain size of SWCNTs. This characteristic size reflects the average mean free path of low-momentum phonon scattering. The characterization itself involves measuring the thermal reffusivity of SWCNT bundles in the axial direction down to 77 K and determining the residual value at the 0 K limit. This residual value reflects the sole structure-phonon scattering due to vanishing Umklapp scattering. We obtain the average structure thermal domain sizes of two SWCNT bundles, which are 46.0 and 61.9 nm. Since there is no other characteristic size information available to compare for SWCNTs, we compare the structure thermal domain size of other micro-/nanoscale materials with their crystallite size by X-ray diffraction to interpret our results.

INTRODUCTION

Since the discovery of carbon nanotubes (CNTs) in 1991,[1] extensive attention has been paid to them due to their unique structure and significant mechanical, thermal, electrical, and optical properties.[2–5] Due to their remarkable physical properties, they have broad applications such as field emission electron sources,[6,7] nanoelectronic transistors,[8,9] sensors,[10–12] energy conversion and storage,[13–16] etc. Among all CNTs, single-walled CNTs (SWCNTs) show preferable electrical properties for great potential applications.[17] The electrical conductivity of SWCNTs is affected by their chirality, which is determined by the chiral vector (n, m).[18,19] There are various techniques to characterize CNT structures, such as X-ray diffractometry (XRD), energy-dispersive X-ray spectroscopy (EDS), scanning electronic microscopy (SEM), transmission electron microscopy (TEM), atomic force microscopy (AFM), and Raman spectroscopy. Soleimani et al.[20] determined the structure, crystal size, and interlayer spacing of MWCNTs using XRD. Their results showed that the XRD pattern of MWCNTs was very similar to that of graphite. Tan et al.[21] used XRD to study the crystalline structure and intershell spacing and TEM to study the physical structure of MWCNTs. Khanbolouki and Tehrani[22] investigated the macroscopic structure of a few-walled CNT yarn using SEM and studied both macroscopic and microscopic structure down to the atomic level using EDS. Using AFM, SEM, and EDS, Nagy et al.[23] compared the structures of CNTs in terms of diameter and length, including SWCNTs and multi-walled CNTs (MWCNTs) synthesized using different processes.

[1]Department of Mechanical Engineering, Iowa State University, Ames, IA 50011, USA

[2]Research Center for Industries of the Future, Key Laboratory of 3D Micro/Nano Fabrication and Characterization of Zhejiang Province, School of Engineering, Westlake University, Hangzhou 310024, P.R. China

[3]These author contributed equally

[4]Lead contact

*Correspondence:
wangtianyu79@westlake.edu.cn (T.W.),
shienzheng@westlake.edu.cn (E.S.),
xwang3@iastate.edu (X.W.)

https://doi.org/10.1016/j.xcrp.2023.101688

CellPress
OPEN ACCESS

Cell Reports
Physical Science
Article

SWCNTs' structure is particularly difficult to characterize due to their single-wall thickness and extremely small diameter. Rarely, an individual SWCNT can have a single-crystalline structure. Although characterizing the structural defects and crystallite size in the axial direction is critical to understanding the energy carrier transport in SWCNTs, it is impossible to measure their crystallite size in this direction, even using grazing incidence XRD to limit penetration into the material and increasing the intensity, due to the extremely small cross-section size of SWCNTs. For powders consisting of SWCNTs, as the size of the SWCNTs and their spacing limit XRD resolution, special sample preparation may be necessary for tubes with smaller diameter. Furthermore, whether the tubes are aligned properly and how many are in the sample might have a strong impact on the XRD results. To date, no crystallite size measurement has been reported on SWCNTs in the axial direction.

To the best of our knowledge, very few studies have been done to obtain the phonon mean free path of SWCNTs. Chang et al.[24] reported the phonon mean free paths of two MWCNTs as 50 and 200 nm. Hepplestone and Srivastava[25] reported the mean free path of 0.46-μm-long (10, 10) SWCNTs as ∼480 nm at 77 K through theoretical calculation, considering longitudinal (LA), doubly degenerate transverse (TA), twist (W), lowest optical (σ), and breathing (в) phonon branches. On the other hand, experimentally determining the mean free path of phonons in SWCNTs remains a big challenge.

In this work, we characterize the average structure thermal domain (STD) size of two highly aligned SWCNT bundles in the axial direction by considering the phonon scattering in different lattice directions using the concept of low-momentum phonon scattering and thermal reffusivity theory. The STD size here reflects the average phonon mean free path induced by defects in the axial direction of SWCNT bundles. Studying the STD size is important for understanding thermal transport properties in materials. A longer mean free path means that phonons travel a greater distance without being scattered, leading to a higher thermal conductivity. In this study, we first measure the thermal diffusivity of highly aligned SWCNT bundles from room temperature (RT) down to 77 K using the frequency-domain energy transport state-resolved Raman (FET-Raman) technique. We also determine the intrinsic average thermal conductivity of SWCNTs. Then, the thermal reffusivity theory is used to study the defect levels and average STD of SWCNTs.

RESULTS AND DISCUSSION

Preparation of highly aligned SWCNTs over trenches via the soft-lock drawing method

CNT films are synthesized using the atmospheric pressure chemical vapor deposition (APCVD) method, utilizing ferrocene/xylene/sulfur as precursor materials. A nickel foil is positioned downstream of a quartz tube to collect the CNT film generated during the CVD process. The CVD furnace is heated to 1,160 °C under 20-sccm Ar gas flow (99.999%). Once the desired temperature is reached, a solution consisting of ferrocene (0.045 g mL^{-1}) and sulfur (0.001 g mL^{-1}) dissolved in xylene is injected into the upstream side of the quartz tube with a flow rate of 5 mL min^{-1}. Simultaneously, the carrier gas is switched to a mixture of Ar and H$_2$ (v$_{Ar}$:v$_{H2}$ = 0.85:0.15) with a flow rate of 1,500 sccm. The reaction time is adjusted from 5 to 60 min to control the thickness of the CNT films. The grown CNT films floating downstream, are collected by the nickel foil. A CNT film can be easily peeled off from the nickel foil and used for other experiments.[26]

To prepare suspended aligned SWCNT arrays over microtrenches, a random SWCNT network film is first transferred and suspended onto a substrate with

**Cell Reports
Physical Science**
Article

CellPress
OPEN ACCESS
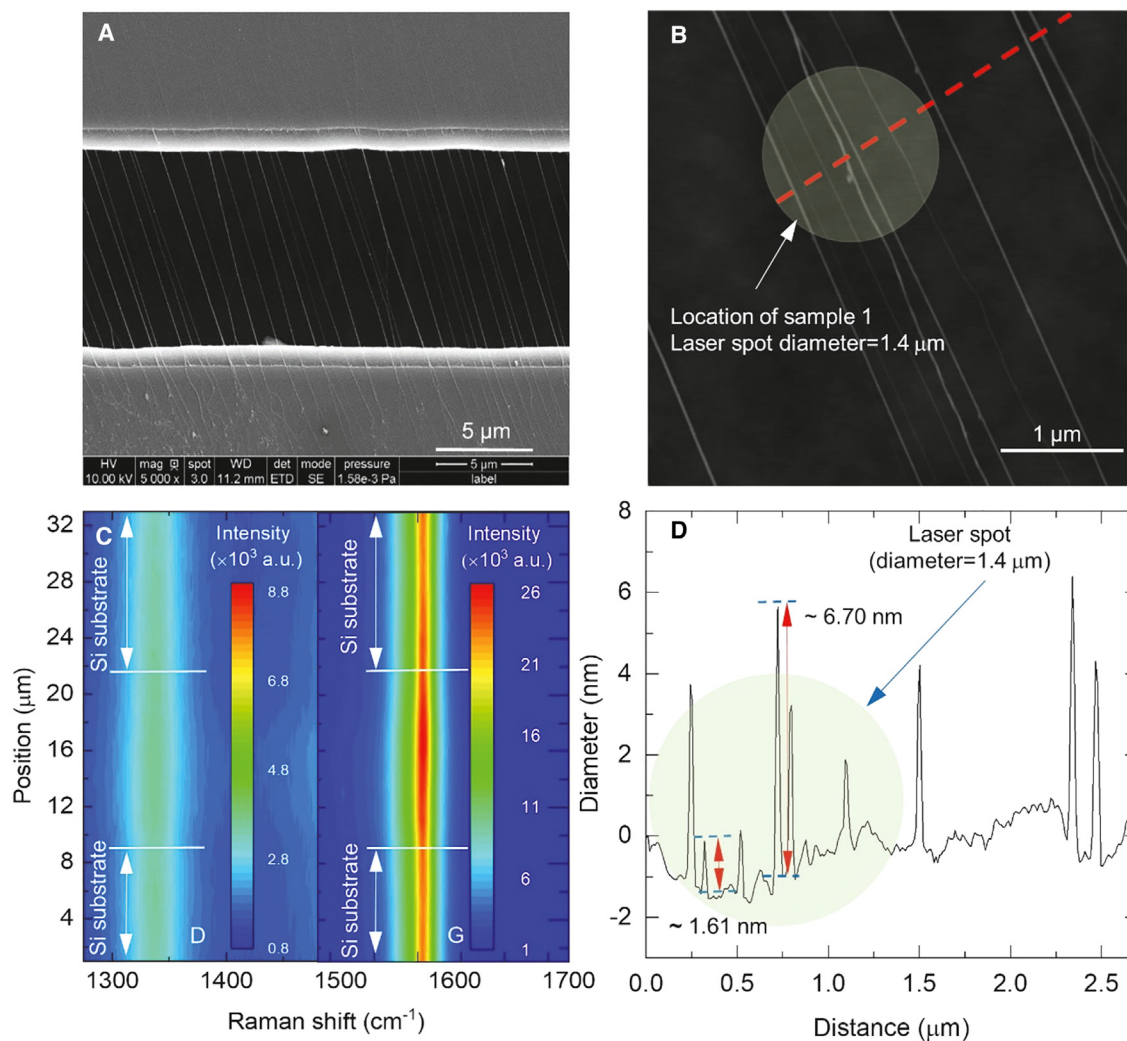
Figure 1. SWCNT sample characterization
(A) SEM image of highly aligned SWCNT bundles under 5,000× magnification. Scale bar: 5 μm.
(B) AFM image of highly aligned SWCNT bundles. Scale bar: 1 μm.
(C) D and G peaks from 1D Raman scanning along the length of sample 1 under 20× objective lens.
(D) Diameter profile of bundles of sample 1 corresponding to the red dashed line in (B). The green shaded circle in (B) and (D) shows the SWCNT region on the substrate whose suspended part is studied using FET-Raman for thermal diffusivity measurement.

microtrenches. Next, a nylon filter film is wetted with ethanol and wrapped around a razor blade. This soft wetted nylon filter film acts as a buffer layer between the blade and the SWCNT network film, which can improve the contact between the SWCNTs and the rigid razor blade and effectively ensure a uniform pulling force on the SWCNTs. Then, the razor blade is pressed against the SWCNT network film on one side of the trench and moved perpendicular to the trench. Under this unidirectional force, SWCNTs are drawn from the network of film, aligned along the pulling force direction, and moved across the microtrenches. Eventually, this results in the formation of suspended aligned SWCNT arrays over the trench.

Sample characterization
Before characterizing thermal diffusivity, we first study the structure of the to-be-measured suspended SWCNT bundles. Figure 1A shows the SEM image of the

CellPress
OPEN ACCESS

Cell Reports
Physical Science
Article

samples under a 5,000× magnification, from which we can see highly aligned SWCNT bundles suspended over a trench in the silicon substrate. We use two SWCNT bundles in this experiment. Their lengths are quite close, 10.08 and 10.36 μm for samples 1 and 2, respectively. Figure 1C shows 1D Raman scanning along the length of sample 1 under a 20× objective lens. Note that the scanning starts from the sample on the silicon substrate and ends on the silicon substrate of the other side of the trench to observe the changes in the D and G peak intensity over the trench. As solid lines represent, both peaks are a little thicker in the position of the sample over the trench. It might be because of the substrate effect. Moreover, since the intensity variation is small through the scanning length, it can be concluded that the sample is quite uniform over the trench. Figure 1B shows the AFM image of the location considered as sample 1. The dashed line represents the location of the diameter profile shown in Figure 1D. The diameters of the SWCNT bundles in that location are in the range of 1.61–6.70 nm. The green circle in Figure 1D represents the laser spot diameter under a 50× objective lens used in our Raman study, which is 1.4 μm ($2r_0$ in the laser beam spatial distribution of $\exp(-r^2/r_0^2)$). It shows that the laser spot covers more than one bundle during FET-Raman measurement. However, since the Raman intensity is proportional to the light-scattering volume and the local laser intensity, the measurement results largely reflect the properties and structures of the thickest bundles, of 6.7 nm diameter for sample 1 and 4.9 nm diameter for sample 2 (not shown in Figure 1).

To study the bundles extensively, Raman scattering is conducted on the bundles measured in this work. The Raman spectrum of sample 1 is shown in Figure 2A. The presence of a D peak (1,344 cm^{-1}) indicates that the sample has defects and it is not a single crystal.[27] The low-frequency peaks at 121, 150, 182, 251, and 265 cm^{-1} are associated with the radial breathing mode (RBM) of SWCNTs. The RBM is related to the radial vibration of carbon atoms. It occurs at low frequencies between 120 and 350 cm^{-1} for SWCNTs with small diameters (d_t), in the range of 0.7 nm < d_t < 2 nm.[28] The Gaussian multiple peaks function is used to fit the RBM peaks as shown in Figure 2B. As mentioned before, RBM is specific to SWCNTs. Therefore, Figures 2A and 2B prove that our CNT sample consists of SWCNTs. RBM can be used to determine the tube diameter.[29,30] Based on the peak locations, the primary diameters of SWCNTs in the bundle are estimated to be 0.84, 0.89, 1.23, 1.49, and 1.85 nm based on the relation $d_t = 223.75 (\text{cm}^{-1}\,\text{nm})/\omega$[30] with ω as the Raman wave number. Therefore, the bundles observed in Figures 1A and 1B consist of many SWCNTs. Moreover, the RBM peaks are fitted using the Gaussian multiple peaks function, as shown in Figure 2B, and their area is analyzed. Note that the contribution to Raman scattering by each peak is roughly proportional to its area under the curve. As can be seen in Figure 2B, since the areas of the Raman peaks at 121 and 182 cm^{-1} are higher than the others, it can be concluded that SWCNTs with the corresponding diameters of 1.85 and 1.23 nm are dominant in the bundle. In addition, since the areas of peaks with Raman wave numbers 251 and 265 cm^{-1} are significantly smaller than the others, we do not consider them in the bundle. Considering the largest-diameter SWCNT bundle of sample 1 (6.7 nm), the estimated number and distribution of individual SWCNTs inside the bundle are shown in Figure 2C. However, this is not the only option for tube distribution and configuration. Therefore, the peak with Raman wave number 121 cm^{-1}, which is related to the SWCNT with a diameter of 1.85 nm (peak in red color in Figure 2B), makes the greatest contribution in the bundle. Similarly, this factor has been considered for two other peaks (green and blue). Based on the AFM results, the SWCNTs shown in Figure 1A are SWCNT bundles with diameters in the range of 1.6–6.7 nm. They consist of individual SWCNTs of diameters 0.84–1.85 nm uncovered by the RBM Raman data. For our samples,

CellPress
OPEN ACCESS
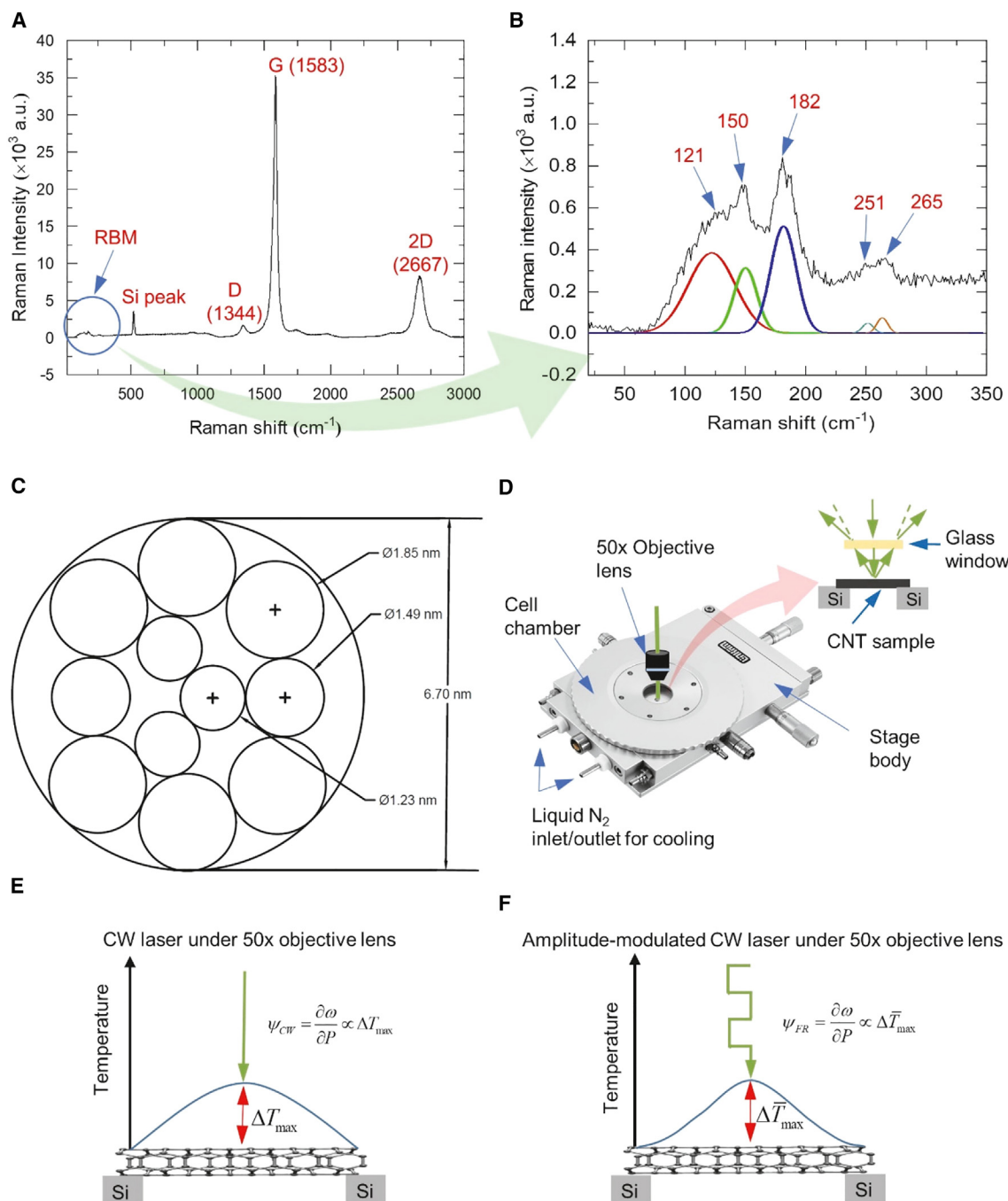
Figure 2. Raman spectrum of SWCNT bundles and FET-Raman physical principle

(A) Raman spectrum of sample 1.

(B) RBM peaks with multi-peak fitting using the Gaussian function.

(C) The estimated distribution of individual SWCNTs with different diameters within the largest SWCNT bundle of sample 1.

(D) Cell chamber for cryogenic measurement down to 77 K.

(E and F) Temperature rise of sample under CW (E) and FR laser heating states (F).

no single SWCNT is observed suspended on the trench, probably due to the large trench width. Future research will focus on suspending single SWCNTs and studying their thermophysical and structural properties using our FET-Raman or ET-Raman.

ə CellPress
OPEN ACCESS

Experimental setup and physical model for thermal diffusivity characterization

The FET-Raman technique[31] is used to measure the thermal diffusivity of the suspended SWCNT bundle from RT down to 77 K. As shown in Figure 2D, the sample is housed inside a cell chamber, which can be positioned by a 3D nanostage (not shown in the figure) so that the laser spot positioning and focusing can be done precisely. An internal block holds the sample while a heating wire and a cooling tube allow the sample to be heated and cooled inside the cell. To cool, nitrogen gas enters the chamber to provide an inert gas environment, and liquid nitrogen is used for cooling. The laser beam (532 nm wavelength) irradiates the sample from the glass viewing window of the cell. Figures 2E and 2F show that the FET-Raman technique uses two different energy transport states as continuous wave (CW) laser and amplitude-modulated laser with a specific frequency (FR) to heat the sample. In both heating states, the laser irradiates the sample, the temperature of the sample rises, and the Raman shift is measured at the same time under different laser powers (P). Then, the Raman shift power coefficient (RSC) of each heating state is measured as $\psi = \partial\omega/\partial P$.[32] In the CW case, its RSC is dependent on the laser absorption coefficient (α_l), the temperature coefficient of Raman shift ($\partial\omega/\partial T$), and the thermal conductivity (k): $\psi_{CW} = \alpha_l(\partial\omega/\partial T)\cdot f_1/k$. In the FR case, RSC is dependent on α_l, $\partial\omega/\partial T$, k, and volumetric heat capacity (ρc_p): $\psi_{FR} = \alpha_l(\partial\omega/\partial T)\cdot f_2(\alpha)/(\rho c_p)$. Here f_1 and f_2 are functions determined by the heating condition and sample geometries and α ($= k/\rho c_p$, k is the thermal conductivity, ρ is the density, c_p is the specific heat) is the sample's thermal diffusivity. To eliminate the effect of laser absorption and Raman temperature coefficients, we normalize RSC as $\Phi = \psi_{FR}/\psi_{CW}$. Now, Φ depends only on the thermal diffusivity α ($= k/\rho c_p$) of the sample and can be used to determine it via data fitting.

For steady-state heating, the energy transport governing equation is:[33,34]

$$k\nabla^2 T_{CW} + \dot{q} = 0, \qquad \text{(Equation 1)}$$

where T_{CW} is the temperature rise in the steady state, k is axial direction thermal conductivity, and $\dot{q}$ is the laser-induced Gaussian beam heating as below:[35]

$$\dot{q}(r,z) = (I_0/\tau_L)\exp(-r^2/r_0^2)\exp(-z/\tau_L), \qquad \text{(Equation 2)}$$

where $I_0 = P/\pi r_0^2$ is the laser (entering the sample) power intensity per unit area in the center of the laser spot, r_0 is the characteristic radius of the laser spot, τ_L is the laser absorption depth, which is $\tau_L = \lambda/(4\pi k_L)$,[36] where λ is the laser wavelength (532 nm) and k_L is the extinction coefficient of the sample. Since the sample diameter is very small (a few nanometers), the temperature is uniform in the radial direction. Note that in this work, Equation 2 is only to show how the laser absorption affects the heat conduction. No precise laser energy absorption evaluation is needed, since the laser absorption information is eliminated in the Φ calculation. However, the laser absorption distribution along the sample ($\exp(-r^2/r_0^2)$) is precisely considered in our data processing and modeling.

For the amplitude-modulated state, the energy transport governing equation is:[37]

$$k\nabla^2 T_{FR} + \dot{q} = \rho c_p(\partial T_{FR}/\partial t), \qquad \text{(Equation 3)}$$

where T_{FR} is the temperature rise in the transient state and $\dot{q}$ could be calculated as in Equation 2, but is square-modulated with 50% duty cycle at frequency f.

SWCNTs are suspended over a trench on a silicon substrate. Silicon can be considered a heat sink in both ends of the sample. Therefore, we consider the sample's
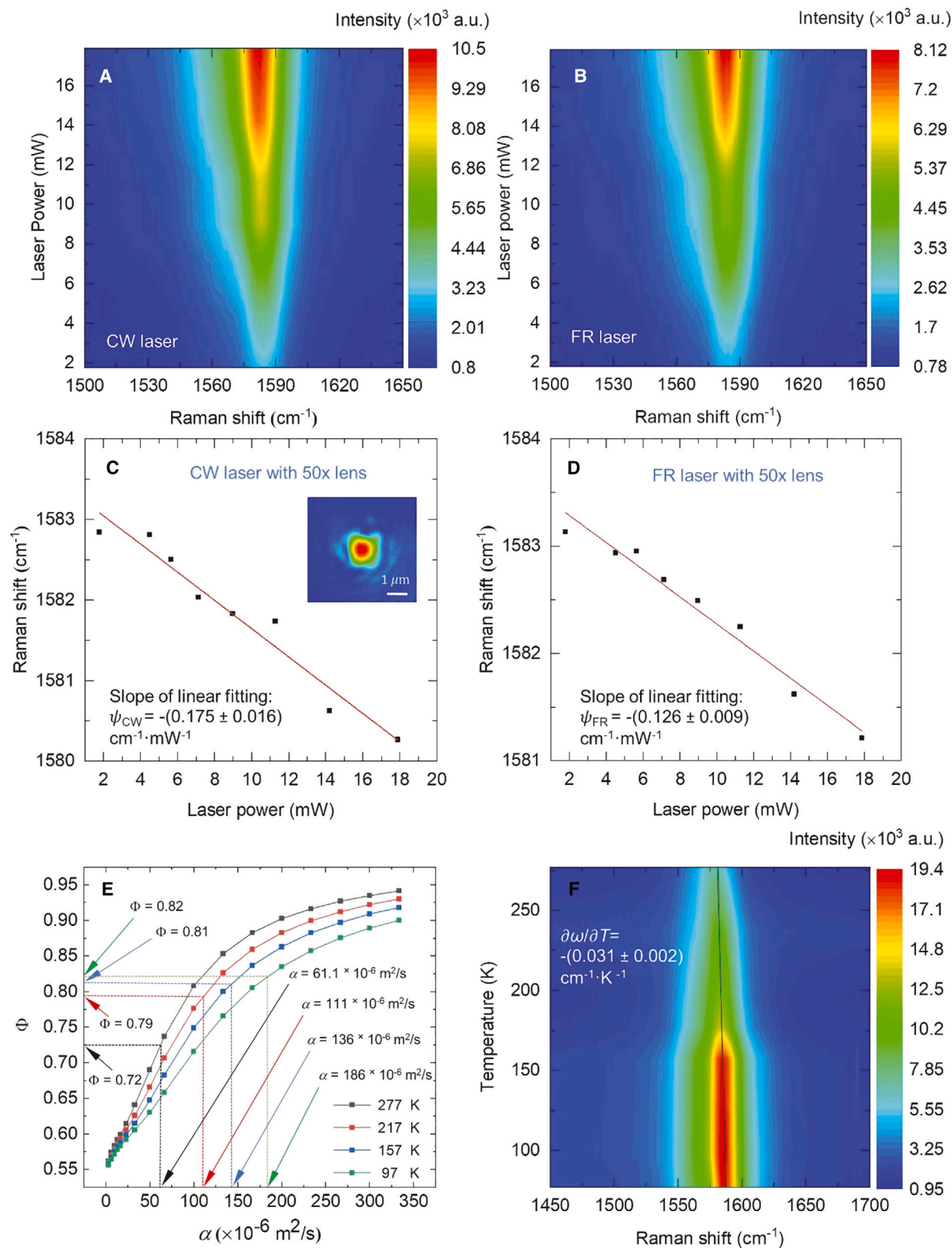
Figure 3. Red shift of SWCNT bundles and their thermal diffusivity determination at different temperatures
(A and B) 2D contour plots of the Raman shift for the G peak against laser power at 277 K for sample 1 for CW (A) and FR laser states (B).
(C and D) Raman shift for the G peak as a function of laser power under a 50× objective lens at 277 K for sample 1 for CW (C) and FR laser heating states (D). The solid line represents the linear fitting to determine RSC, and the inset is the laser spot of the CW laser. Scale bar: 1 µm.
(E) Data fittings of experimental Φ at four different temperatures (97, 157, 217, and 277 K) to determine the thermal diffusivity of sample 1. A frequency of 1.7 MHz was used for the experiment at 77–117 K, 1.4 MHz for 137–177 K, 1.2 MHz for 197–237 K, and 1 MHz for 257–297 K.
(F) 2D contour plot to show the variation in Raman shift against temperature for sample 1.

temperature as RT at both ends as the boundary condition. The theoretical ratio of the temperature rise of the sample in the FR case to that in the CW case can be obtained by solving Equations 1 and 3. To obtain the theoretical relation between the ratio of temperature rise and thermal diffusivity, the 1D heat conduction modeling based on the finite volume method is conducted to simulate the temperature rise of the sample under two energy transport states with different trial thermal diffusivities. It should be noted that the Raman intensity weighted average temperature rise over space ($\overline{T}_{CW}$) in the CW case and the Raman intensity weighted temperature rise over space and time ($\overline{T}_{FR}$) in the FR case are proportional to the corresponding ψ_{CW} and ψ_{FR}, respectively. This Raman intensity weighted temperature rise in spatial and temporal domains is carefully considered in our numerical simulation. Note that in the FR case, the sample cannot completely cool down before a new cycle comes in. This is fully considered in our numerical modeling by considering sufficient heating cycles. Usually up to five cycles are sufficient to account for the heat accumulation effect. In our modeling, we obtain $\Phi_t = \overline{T}_{FR}/\overline{T}_{CW}$ for different trial values of α. By fitting Φ_t against the experimental Φ, we could determine the thermal diffusivity of the SWCNT sample.

Thermal diffusivity measurement using FET-Raman
In the Raman experiment, the Raman spectra from RT to 77 K under different laser powers are collected automatically for two samples to obtain the RSC. Note that the two samples are from different locations of the suspended SWCNTs. Temperatures and laser powers are controlled and varied by a Linkam T95 and LNP95 system controller and an automatic neutral filter wheel (model FW212CNEB), respectively. To avoid sample damage and obtain a linear $\omega \sim P$ correlation, the laser power is kept low in both CW and FR heating states. Taking sample 1 as an example, the laser power is scanned from 1.79 to 17.9 mW under a 50× objective lens. Using this range of laser power, the temperature rise is moderate (detailed later). The CW laser is modulated to a square-wave form using an electro-optic modulator (EOM) (model 350-160; Conoptics) under four different frequencies: 1, 1.2, 1.4, and 1.7 MHz. Note that in our measurement, the frequency is selected to make Φ not deviate from 0.75 much to have a high sensitivity of α measurement. Our past work has proved that when Φ is 0.75, the α measurement has the highest sensitivity.[31]

Figures 3A and 3B show the contour plots of the Raman shift for the Raman peak at ~1,582 cm^{-1} (G peak) at 277 K under different laser powers for sample 1 for the CW and FR cases, respectively. Note that the laser power for the FR case is the power during the duty, not the average power over time. The contour shows red shift of the peak with increased laser power. Figures 3C and 3D show the linear dependency of the Raman shift on laser power for sample 1 at 277 K for the CW and FR laser heating states. The RSC is determined as $\psi_{CW} = -0.175 \pm 0.016$ cm^{-1} mW^{-1} and $\psi_{FR} = -0.126 \pm 0.009$ cm^{-1} mW^{-1}, resulting in a normalized RSC (Φ) of 0.72 ± 0.03. Figure 3E shows the theoretical curve of $\Phi \sim \alpha$ for sample 1 at different temperatures under which different frequencies are selected for the FET-Raman. Frequencies of 1, 1.2, 1.4, and 1.7 MHz are used for 257–277, 197–237, 137–177, and 77–117 K, respectively. The Φ values at four different temperatures (97, 157,

CellPress
OPEN ACCESS
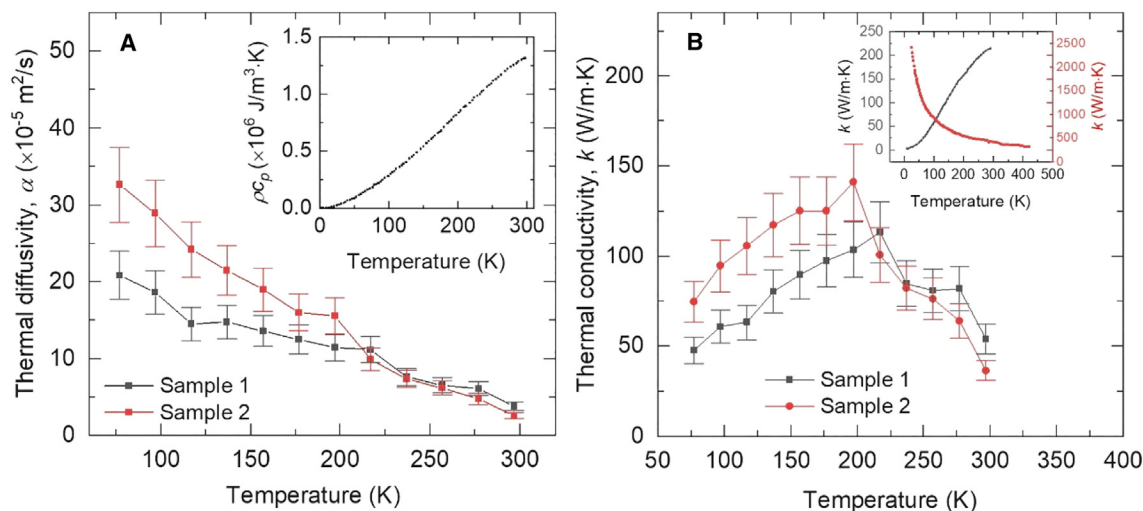
Figure 4. Thermal diffusivity and conductivity variation with temperature
(A) The measured thermal diffusivity for both samples against temperature. The inset is the volumetric heat capacity for the SWCNT wall. The density and specific heat capacity of SWCNT are from the literature.[39,40]
(B) The average intrinsic thermal conductivity of both samples against temperature. The inset is the thermal conductivity of SWCNTs from the literature for comparison. The black line is the work of Hone et al.[48] and the red line is the work of Savin et al.[50] Error bars show the upper bound of uncertainty analysis for measurements.

217, and 277 K) are shown in the figure to interpolate the theoretical curve to determine the corresponding thermal diffusivity. As can be seen, taking Φ at 277 K as an example, the thermal diffusivity of sample 1 is determined as $(6.11 \pm 0.48) \times 10^{-5}$ m^2 s^{-1}. Figure 3F shows the contour plot of the G peak of sample 1 under different temperatures. As can be seen, it indicates the red shift of the peak and decreasing intensity with increased temperature. The temperature coefficient of the Raman shift $(\partial\omega/\partial T)$ is determined as 0.031 cm^{-1} K^{-1} for sample 1. Based on Figures 3C and 3D, at 277 K the largest Raman shift change is about 2.5 and 1.9 cm^{-1} for CW and FR laser, respectively. We estimate the highest temperature rise of sample 1 under CW and FR laser heating $(\Delta T = \Delta\omega/(\partial\omega/\partial T))$ as 81 and 61 K. For the measurement at 77 K, the maximum temperature rise for CW and FR cases is estimated to be 32 and 23 K. This temperature rise is the one in the laser heating location. The whole sample's average temperature rise should be lower, around one-half or lower. Note that the level of laser focusing, laser absorption by the sample, exact location of the laser on the sample, and window reflection might be different at different temperatures. But these do not affect our α measurement accuracy, as the CW and FR laser cases share the same optical configurations. Moreover, to obtain higher temperature sensitivity and experience a lower temperature rise of the sample during laser heating, the resonance Raman ratio (R3) method, first developed by Zobeiri et al.,[38] can be used in future studies.

Thermal diffusivity and conductivity variation with temperature
Figure 4A shows the measured thermal diffusivity for both samples against temperature. As can be seen, the thermal diffusivity increases with decreased temperature. This trend and underlying physics will be discussed in detail later using the thermal reffusivity theory. The volumetric heat capacity is shown in the inset of Figure 4A. Using the density of graphite (2,210 kg m^{-3}) for the wall of the SWCNT[39] and the specific heat capacity of the SWCNT against temperature,[40] the average intrinsic thermal conductivity of SWCNT walls can be obtained. Note that the distance between the graphite layers is 0.34 nm,[27] which is very similar to the wall thickness

**Cell Reports
Physical Science**
Article

of the SWCNT samples, making their densities similar. This average intrinsic thermal conductivity is only for the CNT wall, not considering its hollow space in the middle. The average intrinsic thermal conductivity of both SWCNT samples against temperature is shown in Figure 4B. Phonons instead of electrons contribute the most to the heat conduction in SWCNTs. To explain the thermal conductivity trend, we consider the phonon scattering by the Umklapp process and grain boundaries. Due to the 2D nature of the SWCNT wall, its thermal conductivity can be expressed as $k = \rho c_P v l/2$ under the single relaxation time approximation, where l and v are phonon mean free path and phonon group velocity,[41,42] and ρ is almost constant with temperature. To simplify the expression, thermal resistivity $\rho_{th} \equiv k^{-1}$ is used instead of thermal conductivity k for discussion. Therefore, the thermal resistivity of SWCNTs is expressed by $\rho_{th} = 2/(\rho c_P v l)$. There are two constraints on the phonon mean free path: phonon scattering induced by the Umklapp process (l_U) and defects (l_D) following the Matthiessen's rule $l^{-1} = l_U^{-1} + l_D^{-1}$, assuming the independence of different scattering effects. Consequently, the thermal resistivity can be expressed by $\rho_{th} = 2/(\rho c_P v) \cdot [l_U^{-1} + l_D^{-1}]$. While l_D^{-1} is quite independent of temperature, l_U^{-1} is proportional to the phonon population $e^{-T_D/2T}$,[43] according to the Boltzmann factor, where T_D is the Debye temperature.[44] At near RT, phonon-phonon scattering (Umklapp scattering) dominates thermal transport, so $l_U \ll l_D$. Therefore, the thermal resistivity is determined by l_U^{-1}. By decreasing the temperature, due to the decrease in phonon population, Umklapp scattering gets weak and defects dominate the thermal transport,[45,46] so l_U starts to increase until $l_U \gg l_D$. Therefore, the thermal resistivity is determined by l_D^{-1}. Since l_D^{-1} is quite independent of temperature, the thermal resistivity will be controlled by the specific heat capacity c_P, which decreases with decreased temperature, resulting in increasing thermal resistivity. Consequently, a peak will be observed in the thermal conductivity graph, as shown in Figure 4B. On the right side of the peak, Umklapp scattering dominates the phonon transport. On the left side of the peak, defect scattering controls the phonon transport process more.

Zhu et al.[47] sketched the temperature dependence of the Umklapp process part of thermal resistivity as $\rho_{th,U} = 2/(\rho c_P v) \cdot C e^{-T_D/2T}$, where C is constant, and the defects part of thermal resistivity as $\rho_{th,D} = 2/(\rho c_P v l_D)$, and their sum ρ_{th} for both small and large grain size samples. The approximate factor "2" in "$T_D/2T$" could vary between 2 and 3, depending on the material phonon structure. It is observed that for samples with reduced grain size (higher defect level), l_D^{-1} is increased, resulting in an increase in grain boundary-induced thermal resistivity. As a result, the total thermal resistivity of the reduced grain size sample will increase, and its minimum will be located at a higher temperature. Consequently, the peak of thermal conductivity of the reduced grain size sample will be located at a higher temperature. In this work, a peak in the $k \sim T$ relation for SWCNTs is experimentally observed. To compare our thermal conductivity measurement with those of the literature, we come across the work by Hone et al.,[48] as shown in the inset of Figure 4B, the black line. They measured the thermal conductivity of a bulk sample of SWCNTs in which the tubes were aligned in the parallel direction of heat conduction from RT down to approximately 10 K. Moreover, Hone et al.[49] measured the temperature-dependent thermal conductivity of SWCNTs with a diameter of 1.4 nm from 8 to 350 K (not shown in the figure). No peak was observed in any of $k \sim T$ relations. The reason for that is similar to what has been discussed previously. Increased defect levels push the peak to higher temperatures. Savin et al.[50] reported modeling results on the thermal conductivity of SWCNTs, as shown in the inset of Figure 4B, the red line. However, their k increases all the way to very low temperatures. This means that they did not consider defects in the simulation, and the sample was highly crystalline. Therefore, comparing our

Cell Reports
Physical Science
Article

results to those of the literature, the discrepancy is mainly due to the different structures and level of defects. For the thermal diffusivity and thermal conductivity measurement, the uncertainty is estimated to have an upper bound of 14%, which is shown by error bars in Figure 4. This uncertainty estimation considers the air convection, radiation, and thermal contact resistance between the SWCNT and the Si substrate. Details can be found in the experimental procedures.

### Structure thermal domain size determination based on residual thermal reffusivity

In graphene and similar graphite materials, acoustic phonons sustain the heat conduction.[51] In this section, we use the concept of thermal reffusivity (Θ), first introduced by Xu et al.[52] in our lab as the inverse of the thermal diffusivity, to distinguish and study the defect effects.

Defect level and structure domain size uncovered by residual thermal reffusivity

As mentioned earlier, the thermal reffusivity is the inverse of the thermal diffusivity and is used to study the phonon-defect scattering effect. The thermal reffusivity is influenced only by phonon scattering, and no heat capacity effect is involved. Figure 5A shows the thermal reffusivity of the two SWCNT bundles against temperature down to 77 K. As described before, when the temperature goes down, due to the decrease in phonon population, defects dominate the thermal transport. At 0 K, the Umklapp scattering vanishes, so the thermal reffusivity at 0 K will uncover the defect level and the STD size of the sample in the axial direction. In the case of not having any defects, thermal reffusivity goes to zero at 0 K. The thermal reffusivity consists of two parts, for effects of Umklapp and defects. The Umklapp scattering shows the behavior of $e^{-T_D/2T}$.[44] The thermal reffusivity (Θ) is expressed as:

$$\Theta = \Theta_0 + C \times e^{-T_D/2T}, \qquad \text{(Equation 4)}$$

where C is a constant and T_D is a constant proportional to the Debye temperature. Obviously, with decreased temperature, the thermal reffusivity decreases, and at 0 K, the Umklapp scattering vanishes, and thermal reffusivity reaches a constant Θ_0, which demonstrates the defect scattering. By fitting the data based on Equation 4, we have $\Theta_1 = 6,449 + 2.38 \times 10^6 \times e^{-1445/2T}$ and $\Theta_2 = 4,795 + 1.91 \times 10^7 \times e^{-1898/2T}$, for samples 1 and 2, respectively. T_D is determined to be 1,445 and 1,898 K here, close to that of graphene foam (1,818 K) and pyrolytic graphite (1,133–1,381 K),[53] reflecting great similarity in their structures. For samples 1 and 2, Θ_0 is accordingly determined as 6,449 and 4,795 s m^{-2}, which take 24.5% and 12.3% of the RT thermal reffusivity, respectively. The mean free path of phonons (l_0) induced by defects can be obtained as $l_0 = 2/(v\Theta_0)$, where v is the acoustic phonon velocity at the 0 K limit. Since the chiralities of individual SWCNTs within our bundles are unknowns, we consider SWCNTs of different chiralities of (4, 4), (5, 5), (6, 6), (10, 10), (7, 0), (9, 0), and (11, 0) and calculate their average acoustic phonon velocity at the 0 K limit. Figures 5D and 5E show the typical phonon dispersion relation used in our calculation. This is calculated to be 6.74 km s^{-1}. More details of acoustic phonon velocity calculation can be found in the experimental procedures. Therefore, l_0 is calculated to be 46.0 and 61.9 nm for samples 1 and 2, respectively. Note the phonon mean free path is the average distance that a phonon travels between two consecutive scatterings. l_0 is termed the STD size here, which represents the characteristic size that accounts for the defects on phonon scattering. Note that, since our bundles consist of approximately 11 individual SWCNTs with different chiralities, l_0 is their average STD size. Still, this STD size is the first estimate of the structure domain size in SWCNT and provides deep insight into its structure.
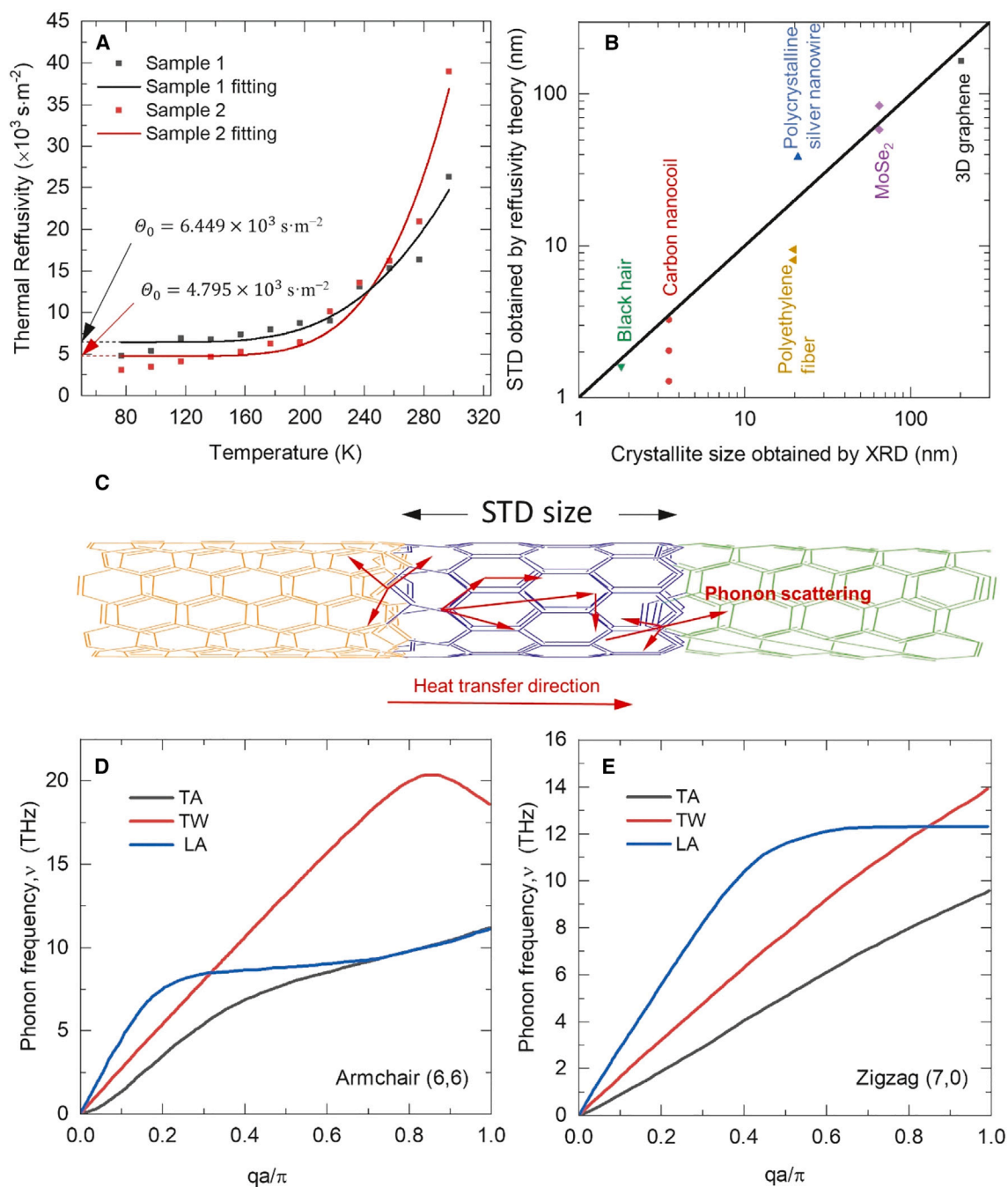
Figure 5. Thermal reffusivity model and phonon scattering as a result of grain boundaries in the axial direction

(A) Variation of the thermal reffusivity against temperature for both samples. The solid lines represent exponential data fitting, and the residual thermal reffusivity at 0 K is also shown for both samples.

(B) Comparison between STD size and crystallite size by XRD for various samples studied in the past.

(C) Schematic showing the phonon scattering by grain boundaries in the axial direction. The arrows indicate the direction of phonon scattering and propagation.

(D and E) The phonon dispersion relation for armchair (6, 6) (D) and zigzag (7, 0) SWCNTs (E), as an example. The lattice constant (a) is 1.667 nm for SWCNTs.[67]

Cell Reports
Physical Science
Article

CellPress
OPEN ACCESS

Figure 5C shows the schematic of phonon scattering by grain boundaries in the axial direction. The arrows indicate the direction of phonon scattering and propagation.

For the average STD size in SWCNTs revealed by our low-momentum phonon scattering, there is no other structural size information available for comparison. However, in our past work on relatively large size (microscale) materials, the STD size has been compared with the crystallite size uncovered by XRD. Here we elaborate on this comparison to provide some in-depth understanding of the STD size. Figure 5B shows the comparison between STD size by reffusivity theory and the crystallite size by XRD of different materials.[43,46,53–56] Note that the solid line represents $y = x$. Overall, the crystallite size from XRD and the STD size from thermal reffusivity theory are quite close to each other. For carbon nanocoils, the XRD size of 3.5 nm is an average for millions of nanocoils, while the STD size is for each individual nanocoils, so it is natural to see deviation of STD size from the XRD crystallite size.[54] For polyethylene microfibers, the crystallite size is 19.7 nm from XRD and their STD size is 8.06 and 9.42 nm.[55] Note that we do not expect that these two methods have exactly the same results, since XRD provides significant information about the sample structure in a specified lattice direction, whereas the reffusivity theory determines the STD size based on phonon scattering from all lattice directions, as shown in Figure 5C. Although the thermal reffusivity is used to measure the phonon scattering behavior for phonon transport in one direction, phonon scattering in all directions contributes to the effective STD size. Furthermore, the thermal reffusivity theory can be used to study the STD size of nanotubes and wires or other materials whose cross-sectional area is too small to induce neutron or X-ray scattering for crystallite size characterization. For amorphous materials, lack of crystalline structure will lead to no peak in beam scattering. Therefore, no structure domain/grain size can be determined. However, the thermal reffusivity theory can still be applied to determine the STD size, since strong phonon scattering can be observed.

In summary, the average STD size of two SWCNT bundles with diameters less than 7 nm was measured using low-momentum phonon scattering and reffusivity theory instead of the XRD technique, since this type of sample induces negligible X-ray scattering in the axial direction due to its extremely small size. Using FET-Raman, the thermal diffusivity of the samples was determined from RT to 77 K, which later was converted to thermal reffusivity. The residual thermal reffusivity at 0 K was determined to be 6,449 and 4,795 s m^{-2} for samples 1 and 2, respectively, which proves the presence of abundant defects in the samples. The corresponding average STD size of samples 1 and 2 was calculated to be 46.0 and 61.9 nm, respectively. For the average STD size in SWCNTs revealed by our low-momentum phonon scattering and thermal reffusivity theory, there is no other structural size information available for comparison. However, in our past work on microscale materials, the STD size has been compared with the crystallite size uncovered by XRD technique. The results showed close agreement but still small differences for certain samples. This is due to the fact that the low-momentum phonon scattering determines the STD size reflecting all lattice directions of phonon scattering, while XRD determines the crystallite size of a specific lattice direction.

EXPERIMENTAL PROCEDURES
Resource availability
Lead contact
Further information and requests for resources and materials should be directed to the lead contact, Xinwei Wang (xwang3@iastate.edu).

CellPress
OPEN ACCESS

Cell Reports
Physical Science
Article

Materials availability
This study did not generate new unique materials.

Data and code availability
Experimental data collected in this work are available upon request. The code for data processing was developed using Fortran and is available upon reasonable request.

Uncertainty analysis

For the SWCNT bundles measured in this work, they have a thermal contact resistance with the Si substrate, which could affect our measurement data. To estimate this effect, the total thermal resistance of one side of the supported SWCNT bundle can be calculated as $R_c = 1/\sqrt{R'^{-1}k_{eff}A_c}$,[39] where R' is the interfacial thermal resistance per unit length of the SWCNT bundle. Note that R' is dependent on the bundle diameter: a thicker bundle will have a lower value due to the larger contact area. Based on our study of R' for different-diameter SWCNT bundles, R' is estimated to be ~800 K m W^{-1} for sample 1 with a diameter of 6.7 nm, as an example. k_{eff} is the effective thermal conductivity of the bundle considering the individual SWCNTs and voids within them, and A_c is the cross-sectional area of the bundle. It should be noted that the supported part of the bundle on a silicon substrate is long enough that it can be assumed to be infinite. Using the estimated number and diameter of individual SWCNTs within the bundle shown in Figure 2C, the total area of individual SWCNTs' walls ($A_{wall\ area}$) can be calculated to find the effective thermal conductivity as $k_{eff} = k \times A_{wallarea}/A_c$. Considering the average intrinsic thermal conductivity (k) of the sample as ~40 W m^{-1} K^{-1} at RT, k_{eff} is calculated to be 17 W m^{-1} K^{-1}. Therefore, the thermal resistance of the supported part (R_c) is calculated to be 1.2×10^9 K W^{-1}. On the other hand, the thermal resistance of the half-suspended bundle can be obtained as $R_{bundle} = (L/2)/(k_{eff}A_c)$ to be 8.4×10^9 K W^{-1} for sample 1, where L is the length of the suspended bundle. Therefore, the suspended sample's thermal resistance is about 7.3 times that of the supported section. This ~14% uncertainty caused by the thermal contact resistance is considered in our uncertainty analysis, as shown by the error bars in Figures 4A and 4B.

To estimate the effect of radiation between SWCNTs and surroundings, we use $\Delta k_{rad} = 16\varepsilon\sigma T^3 L^2/(\pi^2 D)$,[55] where ε, σ, T, L, and D are emissivity, the Stefan-Boltzmann constant, RT, length, and diameter of the SWCNT bundle, respectively. Dawlaty et al.[57] reported the emissivity of six-layer graphene to be ~ 0.03 at a wavelength of 10 μm. Therefore, the emissivity of single-layer graphene is calculated to be 0.005. Taking the presence of 11 individual SWCNTs inside the bundle shown in Figure 2C translates to 22 walls of SWCNT, which causes the emissivity to be around 0.11. The radiation contribution in thermal conductivity for sample 1 at RT, considering the thickest bundle (6.7 nm), is calculated to be 4.14×10^{-3} W m^{-1} K^{-1}. This radiation effect is completely negligible compared with the measured thermal conductivity on the order of 10 s W m^{-1} K^{-1}. In addition, to estimate the effect of convection between SWCNTs and air, we use $\Delta k_{conv.} = 4hL^2/(\pi^2 D)$,[58] where h is the heat transfer coefficient between the SWCNTs and the surrounding air molecules. Hsu et al.[59] reported a heat transfer coefficient of 1.5×10^3 W m^{-2} K^{-1} between air and CNTs with a length of 31 μm and a diameter of 9.89 nm. Note that this heat transfer coefficient is mainly caused by the thermal resistance of an air layer surrounding the SWCNT bundle. This layer's thickness is the air molecule mean free path. Within this layer, Fourier 's law of heat conduction cannot be applied since the continuum assumption does not apply. Instead, the heat transfer is determined by the collisions between air molecules and the SWCNT, as well as the accommodation

Cell Reports
Physical Science
Article

CellPress
OPEN ACCESS

coefficient that is the ratio of the actual energy exchange between the SWCNT and the colliding air molecules to the ideal energy exchange. Mehta and Levin[60] ran a simulation to obtain the energy accommodation coefficient between cold nitrogen and a hot graphene surface. They showed that the tangential energy accommodation coefficient (0.03) is much smaller than that of normal collision (0.61). When the SWCNT bundle is thinner, air molecules collide with the SWCNT atoms in a more tangential way. Also, the rate of collision will decrease substantially. This will make the heat transfer coefficient decrease with the decreased bundle diameter.

Some other studies have been done to predict the heat transfer coefficient between SWCNTs and surrounding air molecules. Among them, Hu et al.[61] reported the interfacial heat conductance as 1×10^5 W m^{-2} K^{-1} between air and one (10, 10) SWCNT with a diameter of 1.34 nm and length of 12.3 nm using molecular dynamics (MD) simulation. Their reported value is larger than the value used in this study (1.5×10^3 W m^{-2} K^{-1} reported by Hsu et al.[59]), since the heat transfer coefficient decreases with increased SWCNT diameter. Our sample is much thicker than those studied by Hu et al.,[61] and this decreases the heat transfer coefficient. Their results also found a very low accommodation coefficient of $\sim$0.02 at 1 atm and RT, which proves our earlier discussion about this coefficient. Wang et al.[62] reported the heat transfer coefficient between an individual CNT and the air in a wide range of diameters using a theoretical model. For a 6.7-nm-thick SWCNT used in this study, the heat transfer coefficient is $\sim$1.07$\times 10^5$ W m^{-2} K^{-1}, which is very close to the maximum value (1.1×10^5 W m^{-2} K^{-1}) corresponding to the accommodation coefficient of unity. However, it is proven that the accommodation coefficient is very low ($\sim$0.02), which will decrease the heat transfer coefficient very much. To eliminate the air convection, future studies should be conducted in a vacuum chamber. This is being planned in our lab and will be conducted in the near future.

Using the reported heat transfer coefficient by Hsu et al.,[59] heat transfer with air will cause an effective thermal conductivity of 9.23 W m^{-1} K^{-1} for sample 1. Note when temperature decreases, the air molecule velocity will decrease, as will the collision rate with the SWCNT bundle. At 77 K, the air heat transfer contribution to thermal conductivity will be reduced to 4.67 W m^{-1} K^{-1}. This is much smaller than the thermal conductivity shown in Figure 4B. Consequently, both radiation and convection have a small effect on the thermal conductivity measurement shown in Figure 4B. For low temperatures, their effect will become more insignificant. Note that, in this work, the air convection will increase the measured thermal conductivity, while the thermal contact resistance with the substrate will decrease the measured thermal conductivity. These two effects could offset each other, and our above 14% uncertainty is a safe upper bound.

Low-energy phonon velocity using phonon dispersion relation

In the structure domain size calculation section, the acoustic phonon velocity at the 0 K limit (low-energy phonon) is required. So here, the low-energy acoustic phonon velocity is discussed and calculated. The phonon dispersion relation of SWCNTs has been extensively investigated.[63–66] Figures 5D and 5E show the phonon dispersion relations of armchair (6, 6) and zigzag (7, 0) SWCNTs, respectively, as examples, where q is the phonon wave number, a is the lattice constant (1.667 nm),[67] and v is the phonon frequency related to phonon energy (E) as $E = hv$. Here, h is the reduced Planck's constant. As can be seen, the three kinds of acoustic phonon modes are TA, LA, and twisting (TW), which have a significant role in heat conduction as they have high group velocity. TA is the lowest-energy acoustic phonon mode, having displacement perpendicular to the tube axis, and doubly degenerates. LA

CellPress
OPEN ACCESS

Cell Reports
Physical Science
Article

Table 1. Phonon group velocities for SWCNTs of different chirality

Type of SWCNT	TA velocity (km s^{-1})	LA velocity (km s^{-1})	Average velocity (km s^{-1})
Armchair (4, 4)	5.8	23.2	7.73
Armchair (5, 5)	4.8	19.1	6.40
Armchair (6, 6)	5.0	24.2	6.80
Armchair (10, 10)	5.0	17.8	6.58
Zigzag (7, 0)	4.8	15.8	6.25
Zigzag (9, 0)	5.9	12.3	7.14
Zigzag (11, 0)	4.9	14.1	6.26

is the higher-energy acoustic phonon mode, having displacement along the tube axis. TW is a rigid rotation around the tube axis driven by the twisting motions of the nanotubes. Note that this acoustic phonon mode is lost in the bundles.[64] Because our sample is bundles consisting of SWCNTs, we do not consider the TW mode in the phonon velocity calculations. Based on the phonon dispersion graphs, the phonon group velocity can be calculated as $v = \partial\omega/\partial q$, where ω is the angular frequency and q is the wave vector. Near the center of the Brillouin zone, at 0 K, the phonon momentum reaches zero. The TA and LA modes have approximately linear dispersion at this location.[68] As a result, the linear slope of each curve near zero q represents v_{TA} and v_{LA} in Figures 5D and 5E. Taking SWCNT (6, 6) as an example, v_{TA} and v_{LA} are 5.00 and 24.2 km s^{-1}, respectively. As Table 1 shows, we calculate the average velocity of phonons as $v_{avg}^{-1} = (2v_{TA}^{-1} + v_{LA}^{-1})/3$ for SWCNTs of different chiralities. Our sample might consist of different chiralities of SWCNTs. However, since there is a small discrepancy among average velocities for different chiralities, we use the average of them as 6.74 km s^{-1}. This might affect the STD size calculation of the SWCNTs, but the effect is insignificant.

AUTHOR CONTRIBUTIONS

Conceptualization, T.W., E.S., and X.W.; methodology, M.R., T.W., E.S., and X.W.; investigation, M.R., B.L., N.H., and I.A.K.; writing – original draft, M.R. and B.L.; writing – review & editing, all authors; funding acquisition, X.W.; resources, T.W., E.S., and X.W.; supervision, T.W., E.S., and X.W.

DECLARATION OF INTERESTS

The authors declare no competing interests.

REFERENCES

1. Iijima, S. (1991). Helical microtubules of graphitic carbon. Nature *354*, 56–58. https://doi.org/10.1038/354056a0.

2. Dresselhaus, M.S., Dresselhaus, G., Charlier, J.-C., and Hernández, E. (2004). Electronic, thermal and mechanical properties of carbon nanotubes. Philos. Trans. A Math. Phys. Eng. Sci. *362*, 2065–2098. https://doi.org/10.1098/rsta.2004.1430.

3. Pint, C.L., Xu, Y.-Q., Moghazy, S., Cherukuri, T., Alvarez, N.T., Haroz, E.H., Mahzooni, S., Doorn, S.K., Kono, J., Pasquali, M., and Hauge, R.H. (2010). Dry contact transfer printing of aligned carbon nanotube patterns and characterization of their optical properties for diameter distribution and alignment. ACS Nano *4*, 1131–1145. https://doi.org/10.1021/nn9013356.

4. Odom, T.W., Huang, J.-L., Kim, P., and Lieber, C.M. (1998). Atomic structure and electronic properties of single-walled carbon nanotubes.

Cell Reports
Physical Science
Article

CellPress
OPEN ACCESS

Nature *391*, 62–64. https://doi.org/10.1038/34145.

5. Hassanien, A., Tokumoto, M., Kumazawa, Y., Kataura, H., Maniwa, Y., Suzuki, S., and Achiba, Y. (1998). Atomic structure and electronic properties of single-wall carbon nanotubes probed by scanning tunneling microscope at room temperature. Appl. Phys. Lett. *73*, 3839–3841. https://doi.org/10.1063/1.122910.

6. Yang, Y., Liu, L., Wei, Y., Liu, P., Jiang, K., Li, Q., and Fan, S. (2010). In situ fabrication of HfC-decorated carbon nanotube yarns and their field-emission properties. Carbon *48*, 531–537. https://doi.org/10.1016/j.carbon.2009.09.074.

7. De Heer, W.A., Bonard, J.M., Fauth, K., Châtelain, A., Ugarte, D., and Forró, L. (1997). Electron Field Emitters Based on Carbon Nanotube Films. Wiley Online Library *9*, 87–89. https://doi.org/10.1002/adma.19970090122.

8. Zhou, Y., Gaur, A., Hur, S.-H., Kocabas, C., Meitl, M.A., Shim, M., and Rogers, J.A. (2004). P-channel, n-channel thin film transistors and p− n diodes based on single wall carbon nanotube networks. Nano Lett. *4*, 2031–2035. https://doi.org/10.1021/nl048950o.

9. Franklin, A.D., Luisier, M., Han, S.-J., Tulevski, G., Breslin, C.M., Gignac, L., Lundstrom, M.S., and Haensch, W. (2012). Sub-10 nm carbon nanotube transistor. Nano Lett. *12*, 758–762. https://doi.org/10.1021/nl203701g.

10. Chopra, S., Pham, A., Gaillard, J., Parker, A., and Rao, A.M. (2002). Carbon-nanotube-based resonant-circuit sensor for ammonia. Appl. Phys. Lett. *80*, 4632–4634. https://doi.org/10.1063/1.1486481.

11. Mittal, M., and Kumar, A. (2014). Carbon nanotube (CNT) gas sensors for emissions from fossil fuel burning. Sensor. Actuator. B Chem. *203*, 349–362. https://doi.org/10.1016/j.snb.2014.05.080.

12. Pavelyev, V.S., Tripathi, N., Mishra, P., Mezhenin, A.V., Kurenkova, Y.G., and Sovetkina, M.A. (2018). CNT-based IR-sensor. J. Phys, Conf. Ser. *1096*, 012127. https://doi.org/10.1088/1742-6596/1096/1/012127.

13. Sun, L., Wang, X., Wang, Y., and Zhang, Q. (2017). Roles of carbon nanotubes in novel energy storage devices. Carbon *122*, 462–474. https://doi.org/10.1016/j.carbon.2017.07.006.

14. Kumar, S., Nehra, M., Kedia, D., Dilbaghi, N., Tankeshwar, K., and Kim, K.-H. (2018). Carbon nanotubes: A potential material for energy conversion and storage. Prog. Energy Combust. Sci. *64*, 219–253. https://doi.org/10.1016/j.pecs.2017.10.005.

15. Dai, L., Chang, D.W., Baek, J.B., and Lu, W. (2012). Carbon nanomaterials for advanced energy conversion and storage. Small *8*, 1130–1166. https://doi.org/10.1002/smll.201101594.

16. Guldi, D.M., Rahman, G.M.A., Prato, M., Jux, N., Qin, S., and Ford, W. (2005). Single-wall carbon nanotubes as integrative building blocks for solar-energy conversion. Angew. Chem. *117*, 2051–2054. https://doi.org/10.1002/ange.200462416.

17. Raval, J.P., Joshi, P., and Chejara, D.R. (2018). Carbon nanotube for targeted drug delivery. Applications of Nanocomposite Materials in Drug Delivery (Elsevier), pp. 203–216. https://doi.org/10.1016/B978-0-12-813741-3.00009-1.

18. Mansouri, M., Vaezzadeh, M., Rezagholipour Dizaji, H., and Saeidi, M.R. (2022). Effect of chirality surfaces overlap on individual carbon nanotubes resistivity. Appl. Phys. *128*, 391. https://doi.org/10.1007/s00339-022-05465-5.

19. Yanagi, K. (2014). Differentiation of carbon nanotubes with different chirality. Carbon Nanotubes and Graphene (Elsevier), pp. 19–38. https://doi.org/10.1016/B978-0-08-098232-8.00003-6.

20. Soleimani, H., Yahya, N., Baig, M., Khodapanah, L., Sabet, M., Burda, M., Oechsner, A., and Awang, M. (2015). Synthesis of carbon nanotubes for oil-water interfacial tension reduction. Oil and Gas Research *1*, 1000104. https://doi.org/10.4172/ogr.1000104.

21. Tan, W.H., Lee, S.L., and Chong, C.T. (2016). TEM and XRD analysis of carbon nanotubes synthesised from flame. Key Eng. Mater. *723*, 470–475. https://doi.org/10.4028/www.scientific.net/KEM.723.470.

22. Khanbolouki, P., and Tehrani, M. (2020). Purification, structural evolutions, and electrical properties of carbon nanotube yarns processed via incandescent annealing. Carbon *168*, 710–718. https://doi.org/10.1016/j.carbon.2020.06.069.

23. Nagy, P., Miklósi, J., Póczik, P., Papp, K., Konya, Z., Kiricsi, I., Pálinkas, G., and Kálmán, E. (2001). Structure comparison of nanotubes produced by different processes. Appl. Phys. A *72*, S185–S188. https://doi.org/10.1007/s003390100665.

24. Chang, C.-W., Okawa, D., Garcia, H., Majumdar, A., and Zettl, A. (2007). Nanotube phonon waveguide. Phys. Rev. Lett. *99*, 045901. https://doi.org/10.1103/PhysRevLett.99.045901.

25. Hepplestone, S., and Srivastava, G. (2007). Low-temperature mean-free path of phonons in carbon nanotubes. J. Phys. Conf. *92*, 012076. https://doi.org/10.1088/1742-6596/92/1/012076.

26. Shi, E., Li, H., Yang, L., Hou, J., Li, Y., Li, L., Cao, A., and Fang, Y. (2015). Carbon nanotube network embroidered graphene films for monolithic all-carbon electronics. Adv. Mater. *27*, 682–688. https://doi.org/10.1002/adma.201403722.

27. Tuinstra, F., and Koenig, J.L. (1970). Raman spectrum of graphite. J. Chem. Phys. *53*, 1126–1130. https://doi.org/10.1063/1.1674108.

28. Dresselhaus, M.S., Dresselhaus, G., Saito, R., and Jorio, A. (2005). Raman spectroscopy of carbon nanotubes. Phys. Rep. *409*, 47–99. https://doi.org/10.1016/j.physrep.2004.10.006.

29. Richter, E., and Subbaswamy, K.R. (1997). Theory of size-dependent resonance Raman scattering from carbon nanotubes. Phys. Rev. Lett. *79*, 2738–2741. https://doi.org/10.1103/PhysRevLett.79.2738.

30. Bandow, S., Asaka, S., Saito, Y., Rao, A.M., Grigorian, L., Richter, E., and Eklund, P.C. (1998). Effect of the growth temperature on the diameter distribution and chirality of single-wall carbon nanotubes. Phys. Rev. Lett. *80*, 3779–3782. https://doi.org/10.1103/PhysRevLett.80.3779.

31. Zobeiri, H., Wang, R., Wang, T., Lin, H., Deng, C., and Wang, X. (2019). Frequency-domain energy transport state-resolved Raman for measuring the thermal conductivity of suspended nm-thick MoSe2. Int. J. Heat Mass Tran. *133*, 1074–1085. https://doi.org/10.1016/j.ijheatmasstransfer.2019.01.012.

32. Hunter, N., Rahbar, M., Wang, R., Mahjouri-Samani, M., and Wang, X. (2022). Determination of a Raman shift laser power coefficient based on cross correlation. Opt. Lett. *47*, 6357–6360. https://doi.org/10.1364/OL.475008.

33. Lee, J.-U., Yoon, D., Kim, H., Lee, S.W., and Cheong, H. (2011). Thermal conductivity of suspended pristine graphene measured by Raman spectroscopy. Phys. Rev. B *83*, 081419. https://doi.org/10.1103/PhysRevB.83.081419.

34. Yuan, P., Liu, J., Wang, R., and Wang, X. (2017). The hot carrier diffusion coefficient of sub-10 nm virgin MoS 2: uncovered by non-contact optical probing. Nanoscale *9*, 6808–6820. https://doi.org/10.1039/C7NR02089A.

35. Wang, R., Wang, T., Zobeiri, H., Yuan, P., Deng, C., Yue, Y., Xu, S., and Wang, X. (2018). Measurement of the thermal conductivities of suspended MoS$_2$ and MoSe$_2$ by nanosecond ET-Raman without temperature calibration and laser absorption evaluation. Nanoscale *10*, 23087–23102. https://doi.org/10.1039/C8NR05641B.

36. Chen, X., and Wang, X. (2011). Microscale spatially resolved thermal response of Si nanotip to laser irradiation. J. Phys. Chem. C *115*, 22207–22216. https://doi.org/10.1021/jp2070979.

37. Sinha, S. (2015). Thermal model for nanosecond laser ablation of alumina. Ceram. Int. *41*, 6596–6603. https://doi.org/10.1016/j.ceramint.2015.01.106.

38. Zobeiri, H., Hunter, N., Xu, S., Xie, Y., and Wang, X. (2022). Robust and high-sensitivity thermal probing at the nanoscale based on resonance Raman ratio (R3). Int. J. Extrem. Manuf. *4*, 035201. https://doi.org/10.1088/2631-7990/ac6cb1.

39. Incropera, F.P., DeWitt, D.P., Bergman, T.L., and Lavine, A.S. (1996). Fundamentals of Heat and Mass Transfer (Wiley).

40. Hone, J., Batlogg, B., Benes, Z., Johnson, A., and Fischer, J. (2000). Quantized phonon spectrum of single-wall carbon nanotubes. Science *289*, 1730–1733. https://doi.org/10.1126/science.289.5485.1730.

41. Armstrong, B.H. (1985). N processes, the relaxation-time approximation, and lattice thermal conductivity. Phys. Rev. B *32*, 3381–3390. https://doi.org/10.1103/PhysRevB.32.3381.

42. Callaway, J. (1959). Model for lattice thermal conductivity at low temperatures. Phys. Rev. *113*, 1046–1051. https://doi.org/10.1103/PhysRev.113.1046.

43. Xie, Y., Zhu, B., Liu, J., Xu, Z., and Wang, X. (2018). Thermal reffusivity: uncovering phonon behavior, structural defects, and domain size. Front. Energy *12*, 143–157. https://doi.org/10.1007/s11708-018-0520-z.

44. Kittel, C., and McEuen, P. (2018). Introduction to Solid State Physics (John Wiley & Sons).

45. Han, M., Liu, J., Xie, Y., and Wang, X. (2018). Sub-µm c-axis structural domain size of graphene paper uncovered by low-momentum phonon scattering. Carbon *126*, 532–543. https://doi.org/10.1016/j.carbon.2017.10.070.

46. Lin, H., Wang, R., Zobeiri, H., Wang, T., Xu, S., and Wang, X. (2021). The in-plane structure domain size of nm-thick MoSe 2 uncovered by low-momentum phonon scattering. Nanoscale *13*, 7723–7734. https://doi.org/10.1039/D0NR09099A.

47. Zhu, B., Wang, R., Harrison, S., Williams, K., Goduguchinta, R., Schneiter, J., Pegna, J., Vaaler, E., and Wang, X. (2018). Thermal conductivity of SiC microwires: Effect of temperature and structural domain size uncovered by 0 K limit phonon scattering. Ceram. Int. *44*, 11218–11224. https://doi.org/10.1016/j.ceramint.2018.03.161.

48. Hone, J., Llaguno, M., Biercuk, M., Johnson, A., Batlogg, B., Benes, Z., and Fischer, J. (2002). Thermal properties of carbon nanotubes and nanotube-based materials. Appl. Phys. A *74*, 339–343. https://doi.org/10.1007/s003390201277.

49. Hone, J., Whitney, M., Piskoti, C., and Zettl, A. (1999). Thermal conductivity of single-walled carbon nanotubes. Phys. Rev. B *59*, R2514–R2516. https://doi.org/10.1103/PhysRevB.59.R2514.

50. Savin, A.V., Hu, B., and Kivshar, Y.S. (2009). Thermal conductivity of single-walled carbon nanotubes. Phys. Rev. B *80*, 195423. https://doi.org/10.1103/PhysRevB.80.195423.

51. Al Taleb, A., and Farías, D. (2016). Phonon dynamics of graphene on metals. J. Phys. Condens. Matter *28*, 103005. https://doi.org/10.1088/0953-8984/28/10/103005.

52. Liu, R., Chen, J., Xun, J., Jiao, K., and Du, Q. (2014). Numerical investigation of thermal behaviors in lithium-ion battery stack discharge. Appl. Energy *132*, 288–297. https://doi.org/10.1016/j.apenergy.2014.07.024.

53. Xie, Y., Xu, Z., Xu, S., Cheng, Z., Hashemi, N., Deng, C., and Wang, X. (2015). The defect level and ideal thermal conductivity of graphene uncovered by residual thermal reffusivity at the 0 K limit. Nanoscale *7*, 10101–10110. https://doi.org/10.1039/C5NR02012C.

54. Deng, C., Sun, Y., Pan, L., Wang, T., Xie, Y., Liu, J., Zhu, B., and Wang, X. (2016). Thermal Diffusivity of a Single Carbon Nanocoil: Uncovering the Correlation with Temperature and Domain Size. ACS Nano *10*, 9710–9719. https://doi.org/10.1021/acsnano.6b05715.

55. Liu, J., Xu, Z., Cheng, Z., Xu, S., and Wang, X. (2015). Thermal conductivity of ultrahigh molecular weight polyethylene crystal: defect effect uncovered by 0 K limit phonon diffusion. ACS Appl. Mater. Interfaces *7*, 27279–27288. https://doi.org/10.1021/acsami.5b08578.

56. Cheng, Z., Liu, L., Xu, S., Lu, M., and Wang, X. (2015). Temperature dependence of electrical and thermal conduction in single silver nanowire. Sci. Rep. *5*, 10718–10812. https://doi.org/10.1038/srep10718.

57. Dawlaty, J.M., Shivaraman, S., Strait, J., George, P., Chandrashekhar, M., Rana, F., Spencer, M.G., Veksler, D., and Chen, Y. (2008). Measurement of the optical absorption spectra of epitaxial graphene from terahertz to visible. Appl. Phys. Lett. *93*, 131905. https://doi.org/10.1063/1.2990753.

58. Rahbar, M., Han, M., Xu, S., Zobeiri, H., and Wang, X. (2023). Development of differential thermal resistance method for thermal conductivity measurement down to microscale. Int. J. Heat Mass Tran. *202*, 123712. https://doi.org/10.1016/j.ijheatmasstransfer.2022.123712.

59. Hsu, I.-K., Pettes, M.T., Aykol, M., Chang, C.-C., Hung, W.-H., Theiss, J., Shi, L., and Cronin, S.B. (2011). Direct observation of heat dissipation in individual suspended carbon nanotubes using a two-laser technique. J. Appl. Phys. *110*, 044328. https://doi.org/10.1063/1.3627236.

60. Mehta, N.A., and Levin, D.A. (2017). Molecular-dynamics-derived gas–surface models for use in direct-simulation monte carlo. J. Thermophys. Heat Tran. *31*, 757–771. https://doi.org/10.2514/1.T4934.

61. Hu, M., Shenogin, S., Keblinski, P., and Raravikar, N. (2007). Thermal energy exchange between carbon nanotube and air. Appl. Phys. Lett. *90*, 231905. https://doi.org/10.1063/1.2746954.

62. Wang, H.-D., Liu, J.-H., Zhang, X., Li, T.-Y., Zhang, R.-F., and Wei, F. (2013). Heat transfer between an individual carbon nanotube and gas environment in a wide Knudsen number regime. J. Nanomater. *2013*, 1–7. https://doi.org/10.1155/2013/181543.

63. Park, J., Lee, J., and Prakash, V. (2015). Phonon scattering at SWCNT–SWCNT junctions in branched carbon nanotube networks. J. Nanoparticle Res. *17*. 59–13. https://doi.org/10.1007/s11051-015-2873-0.

64. Sauvajol, J.-L., Anglaret, E., Rols, S., and Alvarez, L. (2002). Phonons in single wall carbon nanotube bundles. Carbon *40*, 1697–1714. https://doi.org/10.1016/S0008-6223(02)00010-6.

65. Lee, J., Varshney, V., Roy, A.K., and Farmer, B.L. (2011). Single mode phonon energy transmission in functionalized carbon nanotubes. J. Chem. Phys. *135*, 104109. https://doi.org/10.1063/1.3633514.

66. Ye, L.-H., Liu, B.-G., Wang, D.-S., and Han, R. (2004). Ab initio phonon dispersions of single-wall carbon nanotubes. Phys. Rev. B *69*, 235409. https://doi.org/10.1103/PhysRevB.69.235409.

67. Jindal, V., Gupta, S., and Dharamvir, K. (2000). Bulk and Lattice Properties for Rigid Carbon Nanotubes Materials. Preprint at arXiv. https://doi.org/10.48550/arXiv.cond-mat/0008382.

68. Mingo, N., and Broido, D.A. (2005). Carbon nanotube ballistic thermal conductance and its limits. Phys. Rev. Lett. *95*, 096105. https://doi.org/10.1103/PhysRevLett.95.096105.